Geology

Reconstructing magma failure and the degassing network of dome-building eruptions

--Manuscript Draft--

Manuscript Number:	
Full Title:	Reconstructing magma failure and the degassing network of dome-building eruptions
Short Title:	Reconstructing magma failure and degassing network of dome-building eruptions
Article Type:	Article
Keywords:	magma rheology, structural volcanology, strain localisation, permeability, ductile, brittle
Corresponding Author:	Yan Lavallee Ludwig-Maximilians University Munich, Bavaria GERMANY
Corresponding Author Secondary Information:	
Corresponding Author's Institution:	Ludwig-Maximilians University
Corresponding Author's Secondary Institution:	
First Author:	Yan Lavallee
First Author Secondary Information:	
Order of Authors:	Yan Lavallee
	Philip M. Benson
	Michael J. Heap
	Kai-Uwe Hess
	Asher Flaws
	Burkhard Schillinger
	Philip G. Meredith
	Donald B. Dingwell
Order of Authors Secondary Information:	
Manuscript Region of Origin:	GERMANY
Abstract:	Volcanic eruptions are regulated by the rheology of magmas and their ability to degas. Both detail the evolution of stresses within ascending subvolcanic magma. But as magma is forced through the ductile-brittle transition new pathways emerge as cracks nucleate, propagate and coalesce, constructing a permeable network. Current analyses of magma dynamics centre on models of the glass transition, with important aspects such as incremental strain accommodation and (the key monitoring tool of) seismicity, neglected. Here, in a combined methods study, we report the first high-resolution (20 microns) neutron-computed tomography and micro-seismic monitoring of magma failure under controlled experimental conditions. The data reconstruction reveals that a competition between extensional and shear fracturing modes controls the total magnitude of strain-to-failure and importantly, the geometry and efficiency of the permeable fracture network that regulates degassing events. Extrapolation of our findings yields magma ascent via strain localisation along conduit margins, thereby providing an explanation for gas-and-ash explosions along arcuate fractures at active lava domes. We conclude that a coupled deformation-seismicity analysis holds a derivation of fracture mechanisms and network, and its potential application in forecasting technologies.
Suggested Reviewers:	Kelly J.K. Russell Professor, Univeristy of British Columbia jkr2002@gmail.com

	expertise in magma rheology
	Alexandre Schubnel Researcher, Laboratoire de Géologie de l'Ecole normale supérieure aschubnel@geologie.ens.fr expertise in experimental rock mechanics
	Juergen Neuberg Univeristy of Leeds j.neuberg@see.leeds.ac.uk he reviewed the previous version of this manuscript his expertise is in volcano-seismology
	Mickael Laumonier Researcher, Université d'Orléans mickael.laumonier@univ-orleans.fr he reviewed the previous version of this manuscript.his expertise is in experimental magma deformation
	Antonio Costa Univeristy of Reading antonio.costa@ov.ingv.it his expertise is in conduit flow modelling
Opposed Reviewers:	

Cover letter

Click here to download Cover letter: Lavallee - re-appraisal of earlier study_v4.pdf

Reconstructing magma failure and the degassing network of dome-building eruptions

Yan Lavallée[1]
Philip M. Benson[2]
Michael J. Heap[3]
Kai-Uwe Hess[1]
Asher Flaws[1]
Burkhard Schillinger[4]
Philip G. Meredith[5]
Donald B. Dingwell[1]

[1] Earth and Environment, University of Munich, Germany
[2] Earth and Environmental Sciences, University of Portsmouth, United Kingdom
[3] École et Observatoire des Sciences de la Terre, Université de Strasbourg (UMR 7516 Centre National de la Recherche Scientifique), France
[4] Forschungsreaktor FRM-II, Technische Universität München, Garching, Germany
[5] Department of Earth Sciences, University College London, United Kingdom

ABSTRACT

Volcanic eruptions are regulated by the rheology of magmas and their ability to degas. Both detail the evolution of stresses within ascending subvolcanic magma. But as magma is forced through the ductile-brittle transition new pathways emerge as cracks nucleate, propagate and coalesce, constructing a permeable network. Current analyses of magma dynamics centre on models of the glass transition, with important aspects such as incremental strain accommodation and (the key monitoring tool of) seismicity, neglected. Here, in a combined methods study, we report the first high-resolution (20 μm) neutron-computed tomography and micro-seismic monitoring of magma failure under controlled experimental conditions. The data reconstruction reveals that a competition between extensional and shear fracturing modes controls the total magnitude of strain-to-failure and importantly, the geometry and

efficiency of the permeable fracture network that regulates degassing events. Extrapolation of our findings yields magma ascent via strain localisation along conduit margins, thereby providing an explanation for gas-and-ash explosions along arcuate fractures at active lava domes. We conclude that a coupled deformation-seismicity analysis holds a derivation of fracture mechanisms and network, and its potential application in forecasting technologies.

INTRODUCTION

In volcanic systems, the rheology of magmas is of paramount importance. During pre- or syn-eruptive ascent, magmas undergo decompression resulting in crystallization, temperature change, volatile exsolution and degassing (Martel and Schmidt, 2003). Any magmatic gas trapped in the porous network will exert stress against the condensed phases of the magma (melt and crystals), whose resultant deformation is distributed in time via melt rheology. These processes typically result in a nonlinearly depth-dependent magma viscosity, which in turn induces nonlinear ascent dynamics and strain rate variation within the magma column. Such rheological changes are ultimately manifested in eruption style with competition between the characteristic times imposed by the strain rates and the material stress relaxation times posing the volcanic dilemma: "flow or blow" (Dingwell, 1996).

Dome-building eruptions, with their cycles of endogenous and exogenous growth, commonly followed by destruction, epitomise this rapid switch in magma rheology (Hale and Wadge, 2008). Endogenous growth proceeds as long as pervasive viscous and/or plastic deformation mechanisms dominate, but upon strain localisation and shear rupture, growth may proceed exogenously (Watts et al., 2002), generating distinct non-destructive, low-frequency, seismic source signals (Neuberg et al., 2006), which, upon further seismic slip, may erect spine-like structures (Kendrick et al., 2012). The build-up of internal gas pressure is a threat to the structural stability of lava domes (Thomas et al., 2004). Failure of lava domes frequently generates Vulcanian eruptions (Lavallée et al., 2012); in extreme cases dome collapse may lead to severe decompression, triggering catastrophic explosive eruptions (Spieler et al., 2003). The depressurisation path of magma during ascent is controlled by the development of permeability initially via a network of bubbles (Saar and Manga, 1999; Wright and Weinberg, 2009) and then micro-fractures (Mueller et al., 2005), leading to degassing events with contrasting patterns and recurrences (Varley and Taran, 2003). At Santiaguito volcano (Guatemala), for example, the active

dome displays spectacular, hourly gas-and-ash explosions along concentric ring fractures (Johnson et al., 2008), posing tempting questions regarding the geometry of the underlying permeable, degassing network and its relationship to strain localisation in magma (*e.g.*, Jellinek and Bercovici, 2011). Numerical calculations of magma ascent have tested the role of conduit geometry changes (as illustrated by petrographical and field studies; Noguchi et al., 2008) and demonstrated their importance in reducing the confining stress acting on ascending magma and in the creation of both shear and extensional faults (Thomas and Neuberg, 2012). Structural studies of domes partially dissected by explosive eruption provide evidence for the development of these fault types in the roots of domes, which expose pervasive and/or localised permeable networks of faults (Lavallée et al., 2006; Watts et al., 2002).

The fragmentation of magma occurs at the ductile-brittle or "glass" transition (Dingwell, 1996). Although fragmentation is common to all explosive eruptions, the path to fragmentation undoubtedly varies considerably with eruption types. The first analysis of magma failure at the glass transition consisted of the application of a Maxwell body analysis to the viscoelasticity of silicate liquids. In this analysis, the conditions of failure are, for a given liquid chemistry, constrained by temperature and strain rate (Dingwell, 1996). Silicate liquids are Newtonian fluids at low to moderate strain rates, but at the extremely high strain rates anticipated in explosive eruptions, the viscosity becomes non-Newtonian and the liquids will, under conditions of sustained stress, fail in a brittle manner, generating as they do seismicity (Tuffen et al., 2008). This situation is further complicated by the fact that the magmas involved in such eruptions contain crystals; the amount may vary remarkably but their presence is ubiquitous. In conditions that yield Newtonian melt viscosity for pure liquids, crystal-bearing magmatic suspensions may adopt a non-Newtonian, shear-thinning rheology (Lavallée et al., 2007). The presence of crystals also impacts the coefficients of brittle response, with failure typically setting in at strain rates 2-3 orders of magnitude lower than in the crystal-free case (Gottsmann et al., 2009). However, the current lack

of any failure criterion (e.g., Mohr-Coulomb) for magma inhibits failure analyses based on the stress tensor. Recent experimental observations demonstrate that deformation leading to failure is accompanied by a supra-exponential increase in micro-seismicity, measured as acoustic emissions (AE) (Lavallée et al., 2008). Bearing in mind that seismic signals constitute a key indicator of volcanic unrest (Papale, 1999; Scarpa, 2001), and that such information thus has broad impact in hazard mitigation scenarios, the present investigation of magma failure and its associated permeable network incorporated *in situ* AE monitoring. This ensemble of 1) experimental deformation, 2) real-time AE monitoring, 3) ultrasonic testing and, importantly, recent developments in 4) high resolution (20 μm) neutron computed tomography (NCT) imaging places the mechanistic understanding of magma failure and creation of permeable fracture networks in lava domes on a new basis.

MATERIAL AND METHODS

The failure of dome lavas across the ductile-brittle transition – *i.e.*, the non-discrete transition between deformation behaviour considered macroscopically ductile to that considered macroscopically brittle (Rutter, 1986) – was investigated by varying the uniaxial stress imposed on dome lava from Volcán de Colima (with 50-60% crystals and <9% vesicularity) at an eruptive temperature of 940 ºC (Lavallée et al., 2012) (*see supplementary information*). Following previous observations of the onset of cracking in such lavas (at axial stresses ≥20 MPa), experiments were performed at constant stresses of 20, 28, 46 and 76 MPa to assess the total strain-to-failure and monitor the precursory AE activity. The amplitude distribution of recorded AE events was subjected to a statistical analysis analogous to the Gutenberg-Richter seismic *b*-value (*i.e.,* gradient of frequency of occurrence to magnitude) to assess the relative importance of fracture scaling and localisation. The AE data were then subjected to a failure forecast model (Voight, 1988) to test its accuracy across the ductile-brittle transition. For samples in which deformation was arrested

immediately prior to complete failure, we probed the degree of fracturing via porosity and ultrasonic measurements, as well as reconstructed the permeable, fracture network via NCT.

DEFORMATION RESULTS AND REGIMES OF MAGMA

At an applied stress of 20 MPa, magma deformation was macroscopically ductile (i.e., the sample did not succumb to failure within the imposed 35% strain limit); yet the edge of the sample evidenced the growth of pervasive network of fractures (*see Supplementary Information*). In contrast, deformation at higher stresses of 28, 46 and 76 MPa showed an increasingly brittle response manifested by lower total strain-to-failure and lower AE *b*-values (*see Supplementary Information*), indicating a shift from small-scale distributed cracking (*i.e.,* ductile) to large-scale, more localized cracking (*i.e.,* brittle) (Main et al., 1989). The build-up to failure encompassed the nucleation, propagation and progressive coalescence of fractures, accompanied by acceleration in released AE energy. Application of the failure forecast method to the recorded AE energy provided equally accurate forecasts, irrespective of the applied stress and thus total strain (or more importantly, time available) to achieve failure (*see Supplementary Information,* Table S2). This remained true whether we used the complete AE dataset or only the first 50% of recorded AE data. Our initial experimental analyses are therefore generally consistent with field observations, reflecting how transient stress- (and strain rate-) dependent rheologies are driven by the interplay between ductile and brittle components, yielding significant changes in microstructures and, hence, a seismicity-generation mechanism (Main et al., 1989).

Deformation in the brittle regime significantly changes the physical properties of the magma (*see supplementary information*). Optical microscopic analysis revealed an evolution from crystal reorientation and alignment to crystal dislocation and fracturing across the ductile-brittle transition. Specifically, deformation across this transition produced substantial increases in porosity

associated with the development of a dilatant fracture network. This dilatancy also resulted in significant reductions in ultrasonic P- and S-wave velocities of up to 40% and 35%, respectively.

IMAGING THE PERMEABLE FRACTURE NETWORK

The fracture networks developed by the deformation of magma have been imaged via NCT (Fig 1; *see Supplementary Information for videos of 3-D image reconstruction*). In our analysis, each identified fracture was assigned a location and the density of fractures was collapsed onto the sample half space. The geometry of the fracture network was then correlated with the magnitude of the applied stress. Two primary modes of deformation can be recognized over the stress conditions investigated. For deformation at the onset of the ductile-brittle transition (*i.e.*, at an applied stress of 28.5 MPa), we observe a disintegration of the sample through distributed micro- and mesoscopic fractures (Fig 1A, Movie S1A), with axial fractures restricted to within the barrelled section. Crosscutting relationships (seen in Movie S1A) show that axial, extensional micro-fractures first propagated, and were subsequently crosscut by shear fractures at an angle of ~45° from the principal compressive stress (Fig 1A). The axial fractures are wider than the shear fractures thus dominating the development of the porous network. Conversely, for deformation at the brittle end of the ductile-brittle transition (*i.e.*, 76 MPa), the fault structure is characterised by a more localised distribution of macroscopic shear fractures with minor extensional cracks being restricted to the central region of the sample (Fig 1B, Movie S1B). The shear fractures formed a large hourglass shape at an angle of ~20° from the applied compressive stress. In this scenario the macroscopic shear fractures were responsible for the volume increase and the development of a porous network. NCT reveals that nucleation and propagation of fractures is distributed at low applied stresses (and strain rates) whereas failure at high values of applied stresses (and resultant strain rates) develops via strongly localised shear planes.

158 As noted earlier, the key control on degassing at active lava domes lies in the ability of
159 fracture coalescence to create a permeable network. Using the tomographic reconstruction of the
160 permeable fracture network, we assess the permeability (κ) of the experimentally developed shear
161 zones (e.g., Bai et al., 2011; Pan et al., 2010) via the porosity (ϕ) following the relationship
162 (Mueller et al., 2005):

163 $$\kappa = 10^{-17}\ \phi^{3.4} \quad (1).$$

164 This relationship combined with the porous damage induced by shear imaged by NCT provides a
165 first order map of the permeability development during magma failure (Fig 2; *see Supplementary*
166 *Information*). Although the total porosity increase via fracturing were comparable and led to
167 similar bulk permeability increases, analysis of the directional crack density from the NCT
168 highlighted contrasting anisotropy of the fracture networks in the different experiments.
169 Application of the relationship in equation 1 to the imaged crack density illustrates the anisotropy
170 of the permeable fracture network (Fig 2), showing an extreme anisotropy parallel to the direction
171 of applied stress in the sample deformed at 76 MPa, compared to the orthogonal (*i.e.*, lateral)
172 anisotropy of the sample deformed at 28.5 MPa. These distinct constructional scenarios carry
173 important consequences to the ability of magma to degas in upper volcanic conduits and ultimately,
174 achieve fragmentation.
175
176 **AN "ARCHITECTURE" OF MAGMATIC FRAGMENTATION**
177 A reliable forecast of the timing and style of volcanic activity is beyond current methods.
178 Such an approach ultimately requires a thorough understanding of the stress conditions experienced
179 by magma during ascent as well as the mechanics of magma failure, the architecture of the
180 permeable network and its seismic character. The data presented here illustrate some of these
181 relationships. NCT revealed that the stress exerted on the magma controls the style of fractures,

182 expressed in the micro-seismic record via the *b*-value. This fracture style, in turn, controls the
183 development of the fracture network, including the time available to achieve (and thus to forecast)
184 failure. It follows that fragmentation processes proceeding via different ratios of extensional/shear
185 fractures are potentially responsible for the wide range of eruptive styles currently observed at
186 active lava domes. During dome-building eruptions, the flow of crystal-bearing magma is not
187 Hagen-Poiseuille, but that of a plug. Rheologically, the shear thinning nature of magma favours the
188 localisation of strain (and stress) along the conduit margins (Thomas and Neuberg, 2012) as
189 demonstrated by the formation of shear bands in magma near conduit margins and fracture-
190 controlled exogenic growth (Hale and Wadge, 2008). It follows from our experimental analysis
191 that such a strain distribution undoubtedly results in an anisotropic permeable fracture network
192 with variable degassing efficiency (Laumonier et al., 2011), which may in turn reduce the potential
193 for large explosive eruptions (Mueller et al., 2005). Our experiments reveal that magma
194 deformation at the ductile end of the ductile-brittle transition produces a monotonically increasing
195 density of micro-fractures that results in a large volumetric expansion and a pervasive (yet mildly
196 anisotropic) fracture network. At the brittle end of the ductile-brittle transition, deformation
197 proceeds faster and fracturing is more localised, highly anisotropic and sub-parallel to the principal
198 shear direction (Fig 3A). Such contrasting anisotropy of the permeability distribution is likely to
199 strongly influence the pathways for degassing and therefore serves to explain the common
200 occurrence of degassing in periphery of lava domes (Lavallée et al., 2012; Varley and Taran, 2003)
201 as well as ash-and-gas venting along a ring fracture as seen at Santiaguito volcano (Fig 3B).

202 In the implementation of magma rheology to eruptive models, our experimental results
203 suggest that a Maxwell-based approximation of failure cannot explain the strain-dependence of
204 crystal-bearing magma rheology. In practice, however, the findings demonstrate that the time
205 window for forecasting magma failure scales with both the progression timescale and imposed
206 stress. This implies that as long as the source of seismicity is in the magma, forecasting may be

accurate irrespective of explosive eruption style. Indeed, Vulcanian eruptions at slowly growing and deforming lava domes have been forecast (De la Cruz-Reyna and Reyes-Davila, 2001). More recently, there is growing evidence that rapid fracturing processes during sudden collapse of lava domes may also generate sufficient characteristic seismicity to be used as a forecasting proxy (Hammer and Neuberg, 2009). Regardless of the eruption style, fracturing of magma is required for the occurrence of an explosive eruption and the development of models to interpret the architecture of magmatic fragmentation via seismicity is therefore an essential component of any accurate hazard mitigation scheme. We conclude that the combination of experimental magma deformation, AE monitoring and NCT imaging delivers a basis for transferring the conclusions to the field, where deformation and seismic monitoring may ultimately contain the information needed to distinguish not only the timing, but also the style of an impending eruption.

ACKNOWLEDGMENTS

We expressed our gratitude to J. Neuberg and M. Laumonier for their constructive reviews. We acknowledge funding from the DLR, the DFG (LA2651/1-1, LA2651/3-1, HE4565/2-1), PROCOPE (#27061UE), MatWerk, an LMUexcellent Research Professorship as well as the ERC Researcher Grants EVOKES (#247076) and SLiM (#306488).

REFERENCES

Bai, L.P., Baker, D.R., and Hill, R.J., 2011, Permeability of vesicular Stromboli basaltic glass: Lattice Boltzmann simulations and laboratory measurements: Journal of Geophysical Research-Solid Earth, v. 115.

De la Cruz-Reyna, S., and Reyes-Davila, G.A., 2001, A model to describe precursory material-failure phenomena: applications to short-term forecasting at Colima volcano, Mexico: Bulletin of Volcanology, v. 63, p. 297-308.

Dingwell, D.B., 1996, Volcanic dilemma: Flow or blow?: Science, v. 273, p. 1054-1055.

Gottsmann, J., Lavallée, Y., Marti, J., and Aguirre-Diaz, G., 2009, Magma-tectonic interaction and the eruption of silicic batholiths: Earth and Planetary Science Letters, v. 284, p. 426-434.

Hale, A.J., and Wadge, G., 2008, The transition from endogenous to exogenous growth of lava domes with the development of shear bands: Journal of Volcanology and Geothermal Research, v. 171, p. 237-257.

238 Hammer, C., and Neuberg, J.W., 2009, On the dynamical behaviour of low-frequency earthquake swarms
239 prior to a dome collapse of Soufriere Hill volcano, Montserrat: Geophysical Research Letters, v. 36.
240 Jellinek, A.M., and Bercovici, D., 2011, Seismic tremors and magma wagging during explosive volcanism:
241 Nature, v. 470, p. 522-U109.
242 Johnson, J.B., Lees, J.M., Gerst, A., Sahagian, D., and Varley, N., 2008, Long-period earthquakes and co-
243 eruptive dome inflation seen with particle image velocimetry: Nature, v. 456, p. 377-381.
244 Kendrick, J.E., Lavallée, Y., Ferk, A., Perugini, D., Leonhardt, R., and Dingwell, D.B., 2012, Extreme
245 frictional processes in the volcanic conduit of Mount St. Helens (USA) during the 2004-2008
246 eruption: Journal of Structural Geology.
247 Laumonier, M., Arbaret, L., Burgisser, A., and Champallier, R., 2011, Porosity redistribution enhanced by
248 strain localization in crystal-rich magmas: Geology, v. 39, p. 715-718.
249 Lavallée, Y., de Silva, S.L., Salas, G., and Byrnes, J.M., 2006, Explosive volcanism (VEI 6) without caldera
250 formation: insight from Huaynaputina volcano, southern Peru: Bulletin of Volcanology, v. 68, p.
251 333-348.
252 Lavallée, Y., Hess, K.U., Cordonnier, B., and Dingwell, D.B., 2007, A non-Newtonian rheological law for
253 highly-crystalline dome lavas: Geology, v. 35, p. 843-846.
254 Lavallée, Y., Meredith, P., Dingwell, D.B., Hess, K.U., Wassermann, J., Cordonnier, B., Gerik, A., and
255 Kruhl, J.H., 2008, Seismogenic lavas and explosive eruption forecasting: Nature, v. 453, p. 507-510.
256 Lavallée, Y., Varley, N., Alatorre-Ibargüengoitia, M.A., Hess, K.-U., Kueppers, U., Mueller, S., Richard,
257 D., Scheu, B., Spieler, O., and Dingwell, D.B., 2012, Magmatic Architecture of Dome-Building
258 Eruptions at Volcán de Colima, Mexico: Bulletin of Volcanology, v. 74, p. 249-260.
259 Main, I.G., Meredith, P.G., and Jones, C., 1989, A reinterpretation of the precursory seismic b-value
260 anomaly from fracture-mechanics: Geophysical Journal-Oxford, v. 96, p. 131-138.
261 Martel, C., and Schmidt, B.C., 2003, Decompression experiments as an insight into ascent rates of silicic
262 magmas: Contributions to Mineralogy and Petrology, v. 144, p. 397-415.
263 Mueller, S., Melnik, O., Spieler, O., Scheu, B., and Dingwell, D.B., 2005, Permeability and degassing of
264 dome lavas undergoing rapid decompression: An experimental determination: Bulletin of
265 Volcanology, v. 67, p. 526-538.
266 Neuberg, J.W., Tuffen, H., Collier, L., Green, D., Powell, T., and Dingwell, D., 2006, The trigger
267 mechanism of low-frequency earthquakes on Montserrat: Journal of Volcanology and Geothermal
268 Research, v. 153, p. 37-50.
269 Noguchi, S., Toramaru, A., and Nakada, S., 2008, Relation between microlite textures and discharge rate
270 during the 1991-1995 eruptions at Unzen, Japan: Journal of Volcanology and Geothermal Research,
271 v. 175, p. 141-155.
272 Pan, J.-B., Lee, C.-C., Lee, C.-H., Yeh, H.-F., and Lin, H.-I., 2010, Application of fracture network model
273 with crack permeability tensor on flow and transport in fractured rock: Engineering Geology, v.
274 116, p. 166-177.
275 Papale, P., 1999, Strain-induced magma fragmentation in explosive eruptions: Nature, v. 397, p. 425-428.
276 Rutter, E.H., 1986, On the nomenclature of mode of failure transitions in rocks: Tectonophysics, v. 122, p.
277 381-387.
278 Saar, M.O., and Manga, M., 1999, Permeability-porosity relationship in vesicular basalts: Geophysical
279 Research Letters, v. 26, p. 111-114.
280 Scarpa, R., 2001, Volcanology - Predicting volcanic eruptions: Science, v. 293, p. 615-616.
281 Spieler, O., Alidibirov, M., and Dingwell, D.B., 2003, Grain-size characteristics of experimental pyroclasts
282 of 1980 Mount St. Helens cryptodome dacite: effects of pressure drop and temperature: Bulletin of
283 Volcanology, v. 65, p. 90-104.
284 Thomas, M.E., and Neuberg, J., 2012, Conditions for magma failure along variable conduits at Montserrat:
285 Geology.
286 Thomas, M.E., Petford, N., and Bromhead, E.N., 2004, The effect of internal gas pressurization on volcanic
287 edifice stability: evolution towards a critical state: Terra Nova, v. 16, p. 312-316.
288 Tuffen, H., Smith, R., and Sammonds, P.R., 2008, Evidence for seismogenic fracture of silicic magma:
289 Nature, v. 453, p. 511-514.

290 Varley, N.R., and Taran, Y., 2003, Degassing processes of popocatepetl and Volcan de Colima, Mexico, *in*
291 Oppenheimer, C.P.D.M.B.J., ed., Volcanic Degassing, Volume 213: Geological Society Special
292 Publication, p. 263-280.
293 Voight, B., 1988, A Method for Prediction of Volcanic-Eruptions: Nature, v. 332, p. 125-130.
294 Watts, R.B., Herd, R.A., Sparks, R.S.J., and Young, S.R., 2002, Growth patterns and emplacement of the
295 andesitic lava dome at Soufriere Hills Volcano, Montserrat, *in* Druitt, T.H., and Kokelaar, P., eds.,
296 Eruption of Soufriere Hills Volcano, Montserrat, from 1995 to 1999, Geological Society of London
297 Memoir, p. 115-152.
298 Wright, H.M.N., and Weinberg, R.F., 2009, Strain localization in vesicular magma: Implications for
299 rheology and fragmentation: Geology, v. 37, p. 1023-1026.
300

Figure Captions

Figure 1. Fracture networks induced by magma failure. The photograph of each sample is accompanied by the NCT reconstructions of the fracture network (below) and the modelled density of fractures (colour coded where red is heavily fractured and blue is intact) represented in a half space (right). (A) The sample deformed at 28.5 MPa show a pervasive distribution of tensional fractures with predominance in the barrelled area. Shear fractures focus along an hourglass shape at an angle of ~45° from the principal compressive stress. (B) The sample deformed at 76 MPa developed strongly localised shear fractures along an hourglass geometry at an angle of ~20° from the principal compressive stress.

Figure 2. Permeability evolutions during magma failure. The permeabilities κ_{bulk}(before) and κ_{bulk} were modelled from their relationship with the measured porosity as provided by Mueller et al. (2005). Permeability estimates in the axial (κ_{axial}) and lateral ($\kappa_{lateral}$) directions of the deformed samples were derived through assessment of the crack density obtained by the NCT images. The data suggest an increased anisotropy with deformation across the ductile-brittle transition.

Figure 3. Architecture of permeable fracture network induced by strain localisation in magma. A) Schematic of fracture distribution as well as the directional anisotropy of the permeable fracture network which may control degassing (red arrows) during dome-building eruptions. Localisation of strain against the conduit margin induces an increase in permeability, promoting outward degasing towards the conduit margins, regions where the magma is subjected to the highest strain rate, causing fractures sub-parallel to the flow direction, which favour the ascent of gas along larger peripheral fractures. Such a fracture geometry may explain B) the formation of gas-and-ash venting along ring structures at Santiaguito volcano, Guatemala (Photographer: Richard Roscoe).

Figure
Click here to download high resolution image

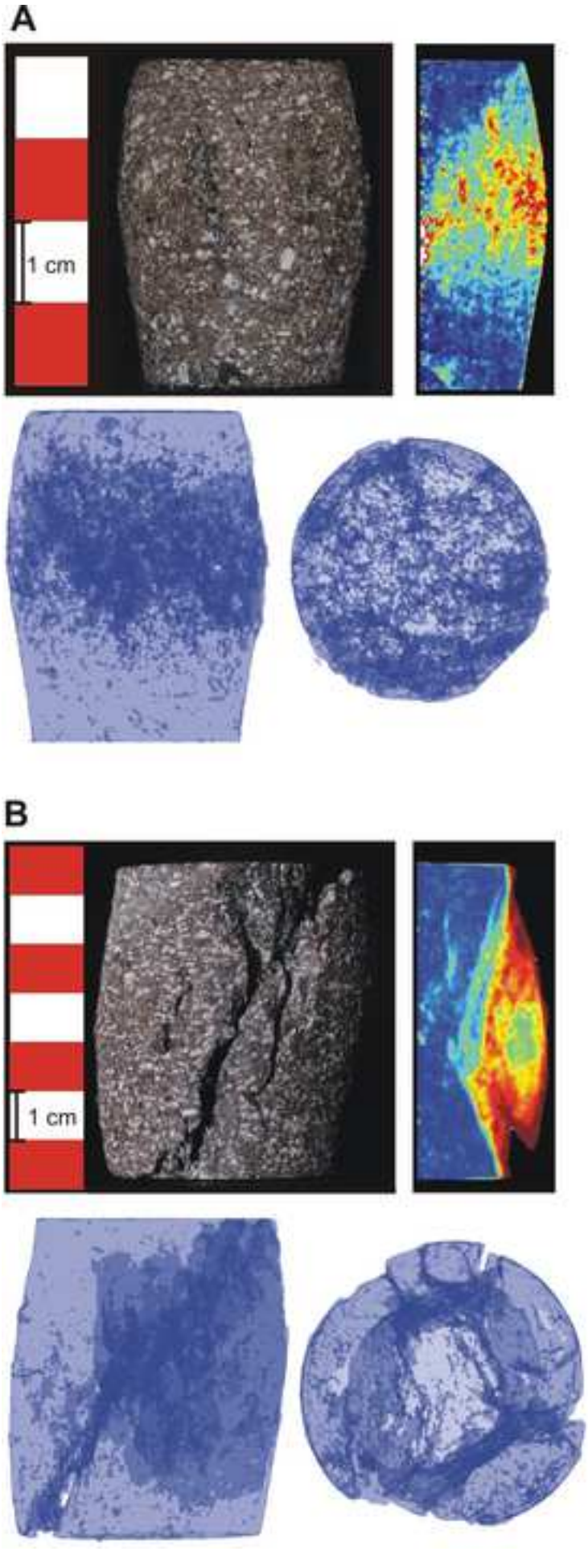

Figure
Click here to download high resolution image

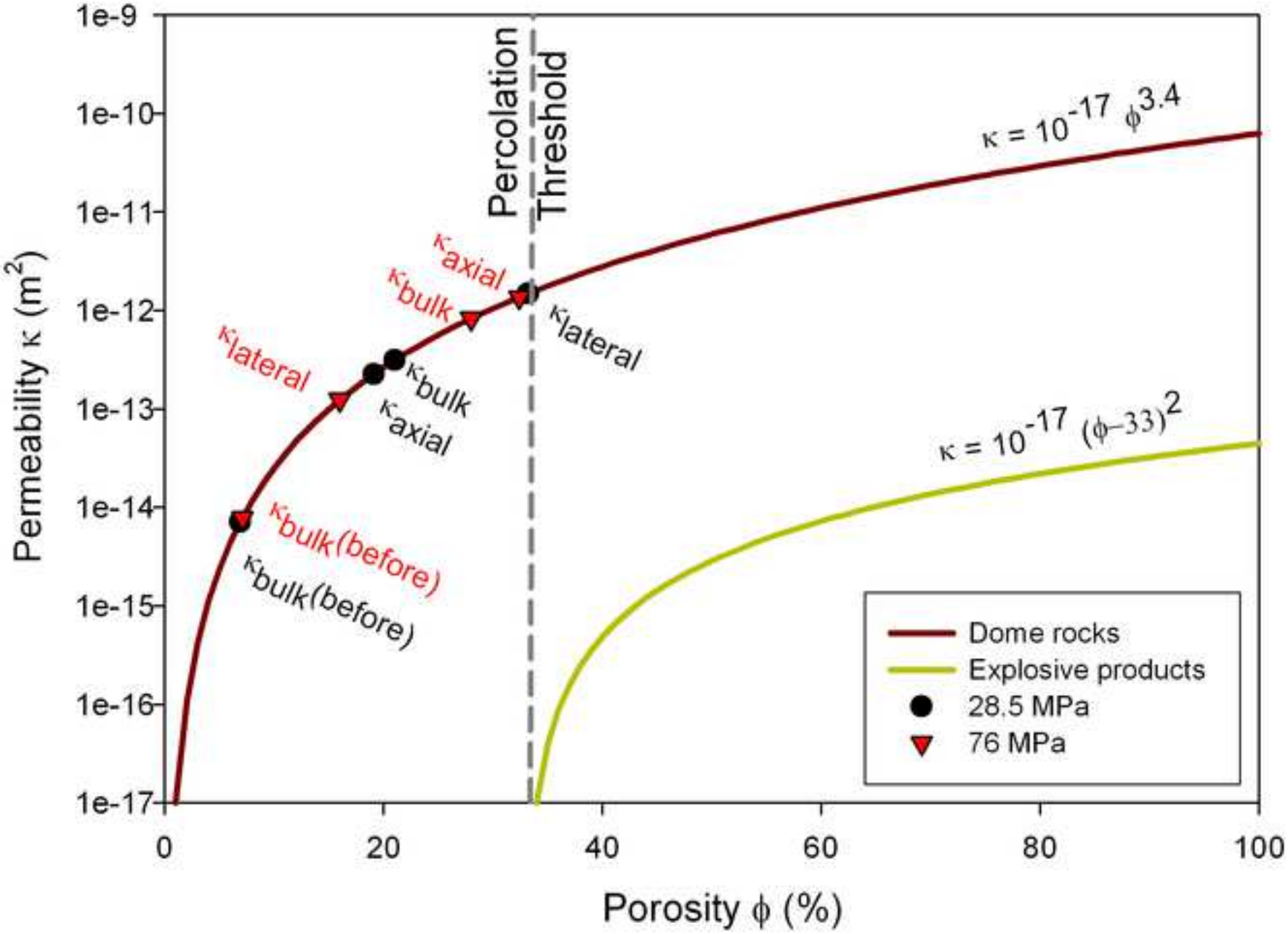

Figure
Click here to download high resolution image

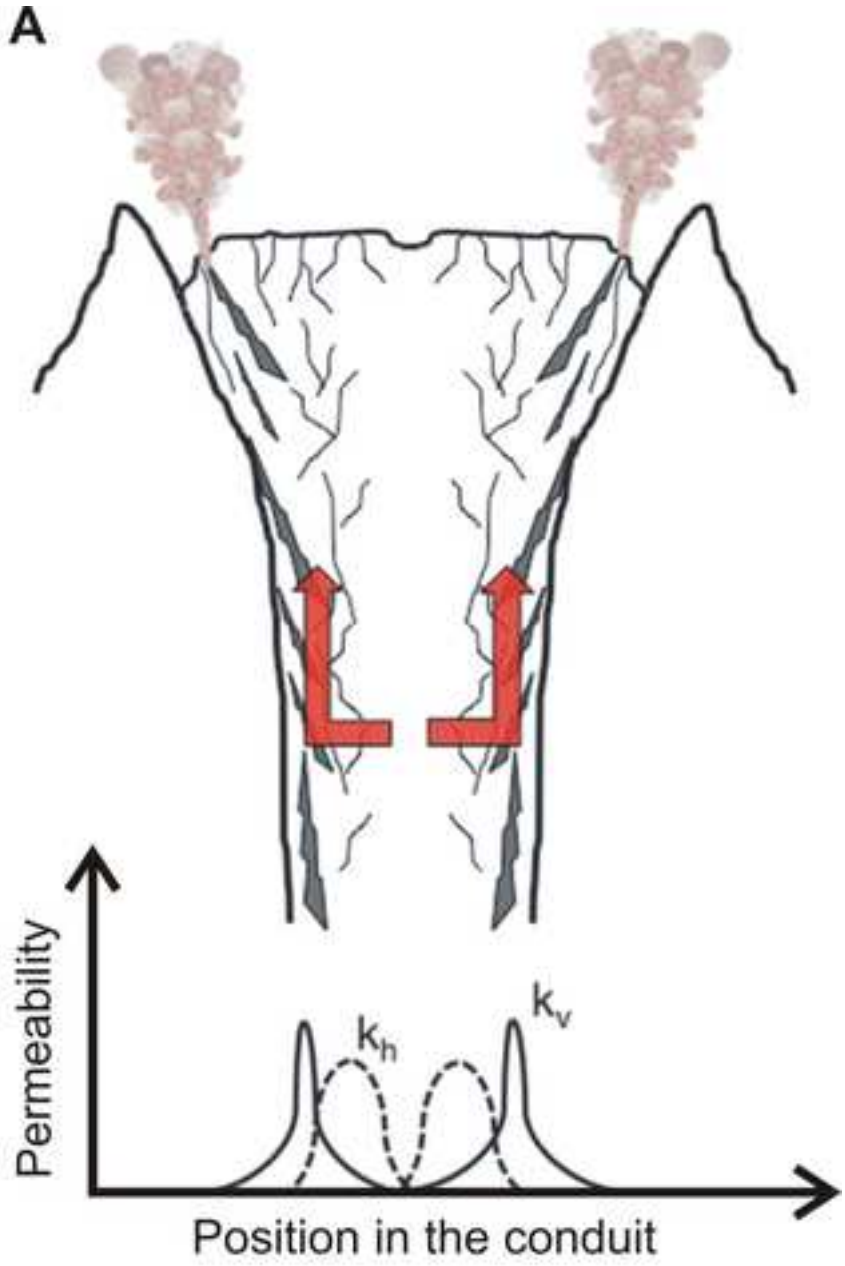

B

Supporting online material

Reconstructing magma failure and the degassing network of dome-building eruptions

1. VOLCANIC MATERIAL

The material chosen was a volcanic rock from dome-building eruptions at Volcán de Colima in Mexico, as extensive experimental work has been performed on this rock type (e.g., Lavallée et al., 2007; 2008; 2012b). The dome rock is an andesite with approximately 55 +/- 5 vol.% of commonly euhedral crystals of plagioclase and pyroxene up to 2.5 mm in length. Embedded microlites showed minor signs of flow alignment, but the crystalline assemblage was characterized as nearly isotropic with an axis ratio of 1.048 (Figure S1; Lavallée et al., 2008). The rock has an average connected porosity of 6.9 vol.% and is highly degassed (≤0.1 ± 0.05%); no volatiles were lost during the extensive heat treatment as confirmed by weight loss tests before and after treatment (Lavallée et al., 2007). Geothermometry has described the pre-eruptive magma condition to 960-1020 °C (Reubi and Blundy, 2008; Savov et al., 2008), whereas the glass transition has been estimated at approximately 710 °C (Lavallée et al., 2012a), although no deformation was experimentally noted below 850 °C (Lavallée et al., 2007).

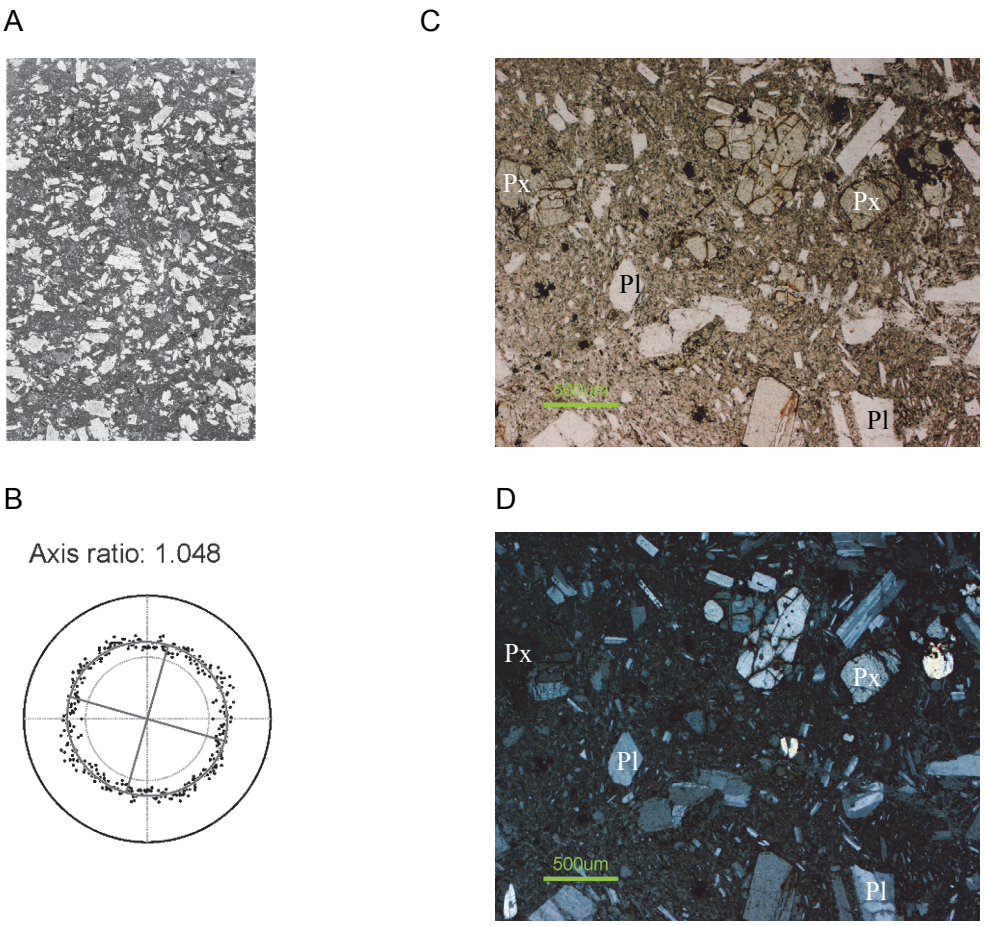

Figure S1. Petrography and microstructures of dome lava samples. (A) Photograph of a thin section (the crystals appears in white and pale grey colours, and interstitial glass as black) from which (B) the anisotropy was measured (Lavallée et al., 2008). The graph is a direction vs slop plot for the intersection of segments with the analysed fabric. Each ring is equivalent to a count of 500 units (see Gerik and Kruhl, 2008). The starting material displays a low anisotropy of 4.8%. Alongside, microphotograph under C) transmitted light and D) cross nickel polarised light show examples of the microstructures present in an original, undeformed sample. Px: pyroxene; Pl: plagioclase

2. DEFORMATION EXPERIMENTS

We have conducted a series of experiments in which dome lavas samples from Volcán de Colima (Mexico) were deformed using a stiff, servo-controlled uniaxial press operating under constant load (<300 kN) and high temperature (<1300 °C), and equipped with a fast-acquisition acoustic monitoring system (Hess et al., 2007; Lavallée et al., 2008) (Fig S2). For the experiments reported here, samples of 50x25 mm and 80x40 mm (length x diameter) were prepared using a diamond coring drill, with the end faces ground flat and parallel to within 0.01 mm. The connected porosity as well as P- and S-wave velocity of the prepared samples was analysed before and after each experiment (see section 4 and 5 below). The samples were placed between the pistons and heated to 940 ± 2 °C using a 12 kW, three-zone split cylinder furnace. After thermal equilibration (over a period of 9 hours), the samples were deformed under constant loads up to different strain increments or until complete failure. Note: Although strain and stress distribution (owing to friction along the sample-piston interface) are not homogeneous throughout the sample (Fig S3), the systematic uniaxial conditions permit the comparison of experimental products with increasing applied stresses.

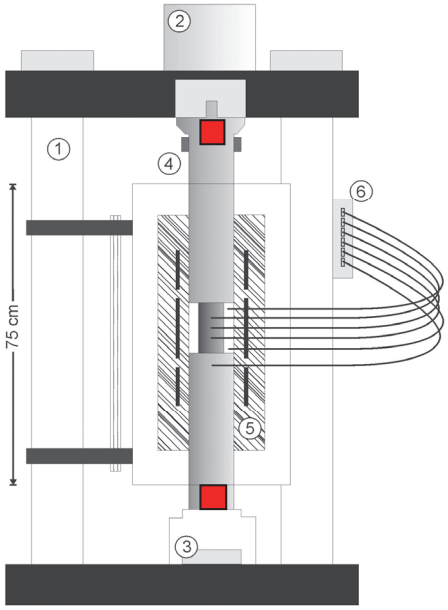

Figure S2. Sketch of the uniaxial press: (1) load frame; (2) servo cylinder with LVDT; (3) load cell; (4) cooling jacket; (5) 3-zone split cylinder furnace; and (6) 6-input thermocouple interface (for type K and S). The red squares show the locations of the AE sensors at the cool ends of the pistons (Modified from Hess et al., 2007).

Here, we focus on moderate to high applied stresses (≥20 MPa) as deformation below such load has been reported to be purely ductile with viscous and plastic components (Lavallée et al., 2007). Such low-stress deformation of magma has been reported to results in constant strain rate and is essentially aseismic, except for the sparse occurrence of AE associated with the sporadic fracture of larger crystals and agglomerations (Lavallée et al., 2008). The porosity and ultrasonic velocity of magma remained largely unchanged by such deformation (see Table S2). Post-experiment microscopic analysis has revealed the reorientation of crystals and a near absence of fracture or crystal dislocation, highlighting the crystal-plastic and viscous nature of magma deformation under these conditions (Lavallée et al., 2008).

Under the range of conditions investigated in this study (≥20 MPa), deformation is accompanied by acceleration in resultant strain rate (Fig S4). With increased applied stresses the strain rate is higher and acceleration faster. Within the imposed strain limit of 35% (see Hess et al., 2007), the sample deformed at 20 MPa did not proceed to fail; although the edge of the sample evidence cracking due to bulging after 20% strain (Fig S3A). Experiments performed at higher applied stresses did succumb to failure.

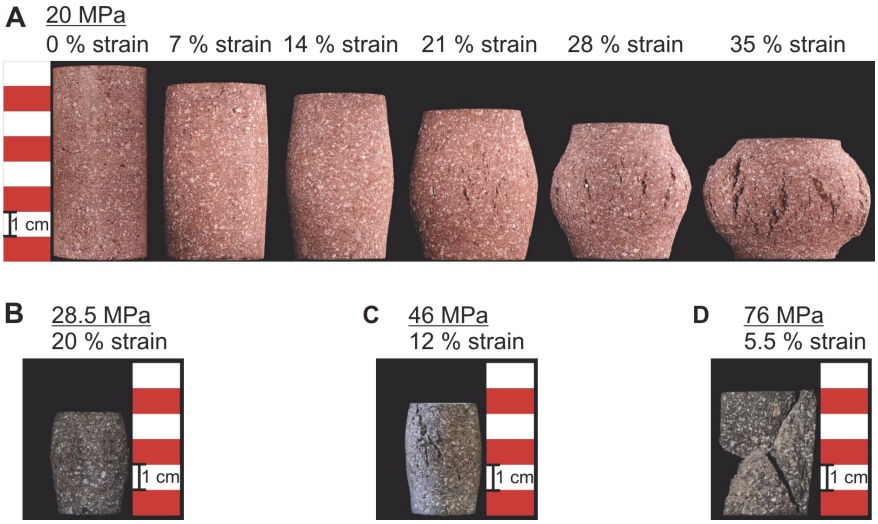

Figure S3. Magma deformation and failure. (A) Strain-step evolution of macroscopic extensional crack propagation during deformation under an applied stress of 20 MPa. Photograph of samples deformed under applies stresses of (B) 28.5 MPa, (C) 46 MPa and (D) 76 MPa.

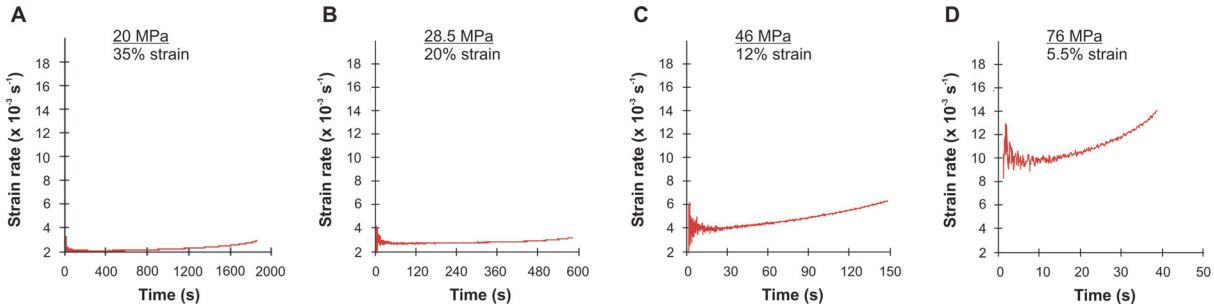

Figure S4. Mechanical response of magma to applied stress. The graphs show the evolution of the strain rate for deformation at applied stresses of A) 20 MPa, B) 28.5 MPa, C) 46 MPa and D) 76 MPa.

3. ACOUSTIC EMISSION MONITORING AND ANALYSIS

Acoustic emissions (AEs) were measured using two piezoelectric transducers (Wideband type WD, Physical Acoustic Corporation) mounted at the end of the loading rams (acting as waveguides). AE signals were pre-amplified by 40 dB and recorded by a fast-acquisition PCI-2 AE recorder at 10 MHz sampling frequency using a triggering criterion of 50 dB simultaneously across both transducers, and with a common event arrival time difference of 150 μs or less.

To further analyse our combined AE dataset, we conducted a seismic *b*-value analysis. In monitoring seismically active regions, one of the most useful analyses to gauge the degree and evolution of fracturing is the seismic *b*-value, defined as the statistical gradient of the number of events of a certain magnitude; that is, the Log(AE frequency)-magnitude distribution (Aki, 1965,

1967). This measure provides a statistical bound on the number of events of a defined size, which – in the laboratory – can be used to ascertain the likelihood of violent and rapid failure or of more benign behaviour; information useful to volcano hazard mitigation (McNutt, 2005). The *b*-value serves to describe the extent of crack propagation, where a general decrease in calculated *b*-values reflects the formation of longer shear planes (Lavallée et al., 2008). Deformation of our samples across the ductile-brittle transition is accompanied by a decrease of the b-value from 3.6 at 28.5 MPa to 2.4 at 76 MPa (Fig S5), which suggests an increased fracture localisation with applied stress. In other word, deformation at higher applied stress generates larger fractures of higher amplitude.

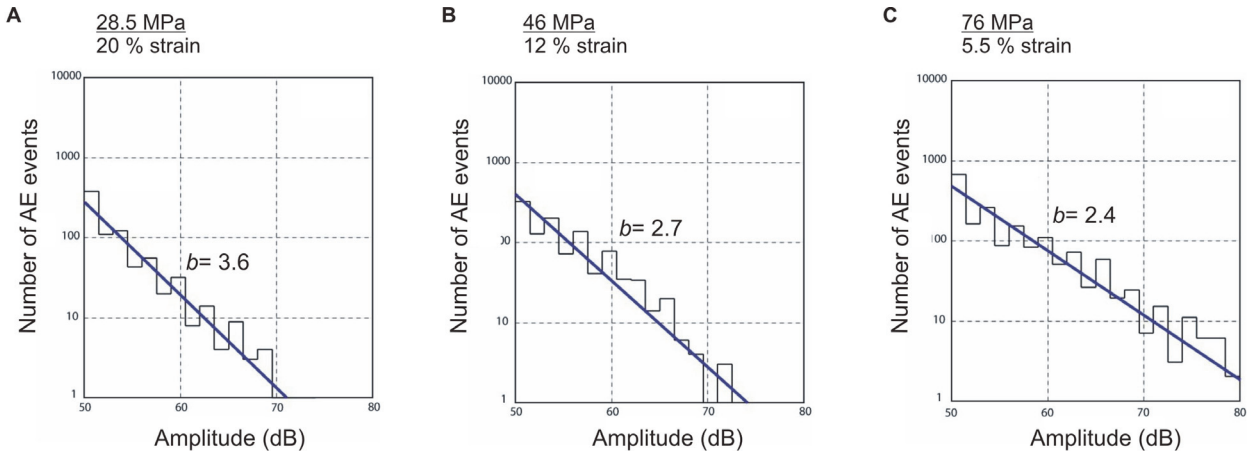

Figure S5. Frequency distribution of acoustic emission event amplitude. The negative slope of the distribution, referred to as the *b*-value, provides a statistical gradient of the size of acoustic events and thus quantitatively assess the relative proportion of small to large fractures. We note that the *b*-value decreases with an increase applied stress

In volcanic hazard assessment, forecasting the timing of an eruption is fundamental to our ability at mitigating the risk. It has recently been suggested that the failure of magma can be forecasted via the failure forecast method (FFM) put forth by Voigth (1988). Here we assess that this method may be applied to the extent of the ductile-brittle transition. The FFM relies on the production rate of precursory phenomena (e.g., seismicity rate, AE rate, seismic energy release, etc.) and correlating their accelerations to the likeliness of failure via the equation

$$\frac{d^2\Omega}{dt^2} = A\left(\frac{d\Omega}{dt}\right)^{\alpha} \quad (1)$$

where $d^2\Omega/dt^2$ and $d\Omega/dt$ are the acceleration and rate of the phenomenon being monitored (here AE), and A and α are empirically determined parameters (Kilburn, 2003; Voight, 1988). More explicitly α is expected to evolve from 1 to 2 before an eruption (Cornelius and Voight, 1995). Recent description of the fracturing time series that arise from random energy fluctuations within a finite volume subject to a constant remote stress proposed that the peaks in event rate (rather than all seismic events) predict best the path to failure and that α = 2 when approaching failure (Kilburn, 2003). The equation can thus be simplified to:

$$\frac{1}{d\Omega/dt} = A\left(t_f - t\right) \quad (2)$$

where t_f is the expected time-to-failure. Since the acceleration increases before failure, the extrapolation of the inverse rate to zero provides the time-to-failure (Fig S6). In our failure analysis, we compared the accuracy using 50% and 100% of the dataset and found equal accuracy of the

method. We find that despite the fact that the time window for forecasting failure at higher applied stress diminishes (Fig S6), the accuracy of the forecast remains whether we use 50% of the data or the whole dataset (Table S1).

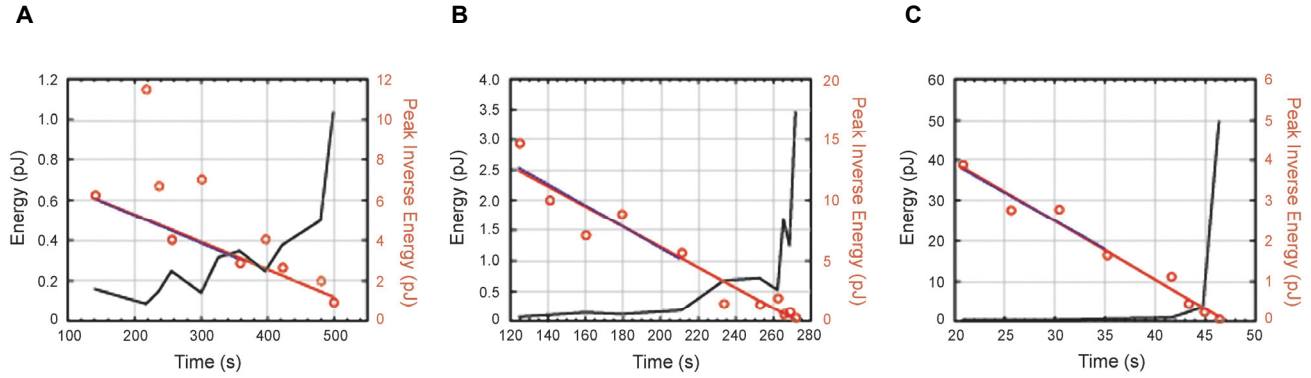

Figure S6. Forecasting magma failure across the ductile-brittle transition. The graphs report the acceleration in released AE energy (black line) for deformation at (A) 28.5 MPa, (B) 46 MPa and (C) 76 MPa. Forecasts are based on the extrapolation (blue and red lines) of peaks in inverted rate of released AE energy (red circles). The inverted peak rates were calculated by binning the number of AE data by time interval for a higher accuracy of the method (Smith and Kilburn, 2010). Comparison of forecast time after 50 % of the deformation (F_{50}; red line) to the forecast time using all inverse seismic rate (blue dotted line) are used to test the accuracy of the method in forecasting the failure of magma (compiled in Table S1). The estimated *b*-value decrease reflects the increasing localisation of crack propagation with increasing applied stress (see Fig S5).

Table S1. Accuracy of the failure forecasts using the AE output from the first 50% strain (F_{50}) and the entire dataset (F_{100}). Variation in accuracy is approximately 0.1 percentage points (based upon 0.1s accuracy)

Applied stress (MPa)	Failure (s)	F_{50} (s)	Accuracy (%)	F_{100} (s)	Accuracy (%)
28.5	587	578.6	1.4	589.3	0.4
46	273	268.8	1.5	273.0	0
76	47	47.8	1.7	47.2	0.4

4. POROSITY DETERMINATION

Porosity values were determined using a helium pycnometer (Micromeritics Accupyc 1330). The measuring method is based on the exact determination of the amount of Helium gas displaced by a samples solid phase volume. Prior to and after each experiment, a weighed sample was placed in a test cell with known volume. The gas pressures observed upon filling the measuring chamber and then discharging it into a second empty chamber allow the determination of volume displaced (V_{pyc}). Since the geometrical volume (V_g) of the cylindrical sample is known, the volumetric fraction of the rock's connected porosity (Φ) can be estimated using

$$\Phi = (V_g - V_{pyc})/V_g \quad (3).$$

In our experiments we observe that, in contrast to deformation in the purely viscous and/or plastic regime at low applied stress (Lavallée et al., 2007), the failure of magma is accompanied by an increase in porosity, although no systematic increase is noted with applied stress (Table S2). We surmise that such a lack of correlation between the applied stress and the changes in the porous

network may reflect the difficulty in arresting the deformation at a comparable total strain prior to failure for each experimental condition.

Table S2. Physical property changes induced by magma deformation. Porosity (Φ) measurements were done at room temperature, using a helium pycnometer (Micromeritics Accupyc 1330). *The porosity of the sample deformed at an applied stress of 76 MPa was exceptionally measured via the Archimedean method as the deformed sample would not fit in the pycnometer. P- and S-wave ultrasonic velocities were measured using a pulsing signal at 50 dB, monitored across the sample by an oscilloscope. The post-experiments values are compared to the average velocities of 3.13±0.03 km/s obtained for the P-waves and 1.55±0.09 km/s obtained for the S-wave of the original rock sample. The measurements were done.

Applied stress (MPa)	Strain (%)	Φ_{before} (%)	Φ_{after} (%)	$\Delta\Phi$ (%)	Vp_{after} (Km/s)	Vs_{after} (km/s)	ΔP- (%)	ΔS- (%)
8	35	6.7	5.7	-1.0	3.03	1.54	-3.2	-0.6
28.5	18	6.9	21.0	+14.1	2.00	1.22	-36.1	-21.3
46	12	7.3	18.2	+10.9	1.87	1.06	-40.3	-31.6
76	5.5	7.1	28.0*	+20.9	1.92	1.01	-38.7	-34.8

5. ULTRASONIC TESTING

Pre- and post-experiment ultrasonic wave velocities were measured via PZT piezoelectric P- and S-wave transducer crystals positioned at each end of the sample, using a Agilent Technologies 1.5GHz 'Infiniium' digital storage oscilloscope and a JSR DPR300 35MHz ultrasonic pulser/receiver. The cylindrical sample was positioned lengthwise between a set of transducers (P or S) and a 900V pulse was discharge from a pulsing transducer across the sample and simultaneously to the oscilloscope. Time of arrivals of P- (or S-) wave to the receiving transducer as well as the length of the sample was used to calculate each ultrasonic velocity.

Deformation in the ductile-brittle transition is accompanied by a decrease in P- and S-wave velocities (Table S2), which may be associated with the creation of damage through fracturing of the samples. In contrast, deformation in the purely viscous and/or plastic regime at low applied stress (Lavallée et al., 2007), results in nearly no changes in ultrasonic velocities.

6. NEUTRON COMPUTED TOMOGRAPHY

The internal structure of the samples was analysed prior to deformation and following failure using a novel neutron computed tomography (NCT) method. This method is identical – in principle – to X-ray computed tomography, which is widely used in medical science, and becoming more popular in the geosciences due to the 3-D, but non-destructive nature of the resulting analysis (Ketcham and Carlson, 2001). The advantage of the neutron over X-ray is that it enables the imaging of large samples up to 36 cm. Imaging was carried out using the ANTARES detector and FRM II cold neutron beam facility installed at Garching, Germany (Hess et al., 2011; Muhlbauer et al., 2005). Reconstructed images from the NCT have a voxel size of approximately 30 μm, easily permitting a 3-D reconstruction of the internal structure of the samples and the extensive fracture patterns produced by the deformation (Hess et al., 2011; King et al., 2008).

7. 3-D RECONSTRUCTION OF THE FRACTURING ARCHITECTURE

Reconstruction videos of the internal fracture networks were produced for samples deformed at 28.5 and 76 MPa (Video 1). The videos show the cross sectional structures, traveling downward through the samples.

A B

Movie S1. Videos of the internal, permeable, fracture network structure of experimentally deformed samples from top to bottom. The crystals and glass show in a grey scale and the fractures show in black. (A) Under 28.5 MPa, radial, extensional cracks dominate the brittle response of the sample. (B) Under 76 MPa, deformation is mainly brittle and primarily forced the propagation of major shear cracks.

8. FRACTURE NETORK DISTRIBUTION

The distribution of fractures was quantified by assessing their geometries and positions. The volume of crack space was delimited by thresholding the greyscale tomography data for the air and simply summing up the voxels together. After identification, the widths of cracks were determined using an n-space Euclidean distance algorithm combined to a topological skeletonisation to find the centre of the crack (e.g., Ma and Sonka, 1996). The distribution of cracks was quantified with respect to their radial orientation – a practice, equivalent to a 2D anisotropy, possible due to the general cylindrical symmetry of cracks produced in a cylindrical sample deformed uniaxially. [This technique works well for the sample deformed at 28.5 MPa. However, for the sample deformed under 76 MPa, the large size of the fractures prevented such a detailed analysis.] For each skeleton line in a 2D cylindrical cross section (Fig S7), the radial extent r and length l are measured and the ratio provides the radial orientation ν.

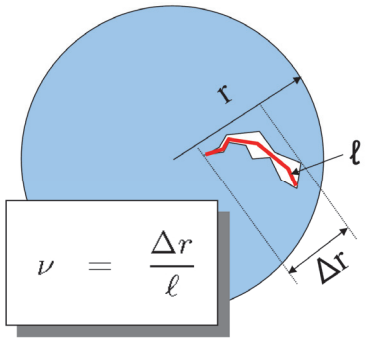

Figure S7. Schematics of fracture dimension quantification. Δr: radial extent, l: length, and ν: the ratio provides the radial orientation.

8.1. Fractures produced during deformation under an applied stress of 28.5 MPa

In a first step, the area of each fracture was estimated (using the amount of black voxels covered), then compared to its vertical position within the sample (Fig S8A). The extensive ductile barrelling of the sample deformed at 28.5 MPa is predominantly fractured in the middle. The width (w) of the fractures was also assessed across each sample; that is, as a function of the ratio of the distance from the centre (r_{cyl}) to length of each crack (L_{crack}). Thin fractures are found everywhere within a section and we observe a preferential widening near the edges of the sample, where barrelling is most important (Fig S8B). Using the orientation of the fractures, we computed the distribution of radial and tangential (shear) fractures and collapsed the density of each fracture type in all direction within a half space (Fig S8C). We observe that the tangential fractures define a hourglass pattern in which extensional fractures preferentially developed in the outside barrelled region (Fig S8D).

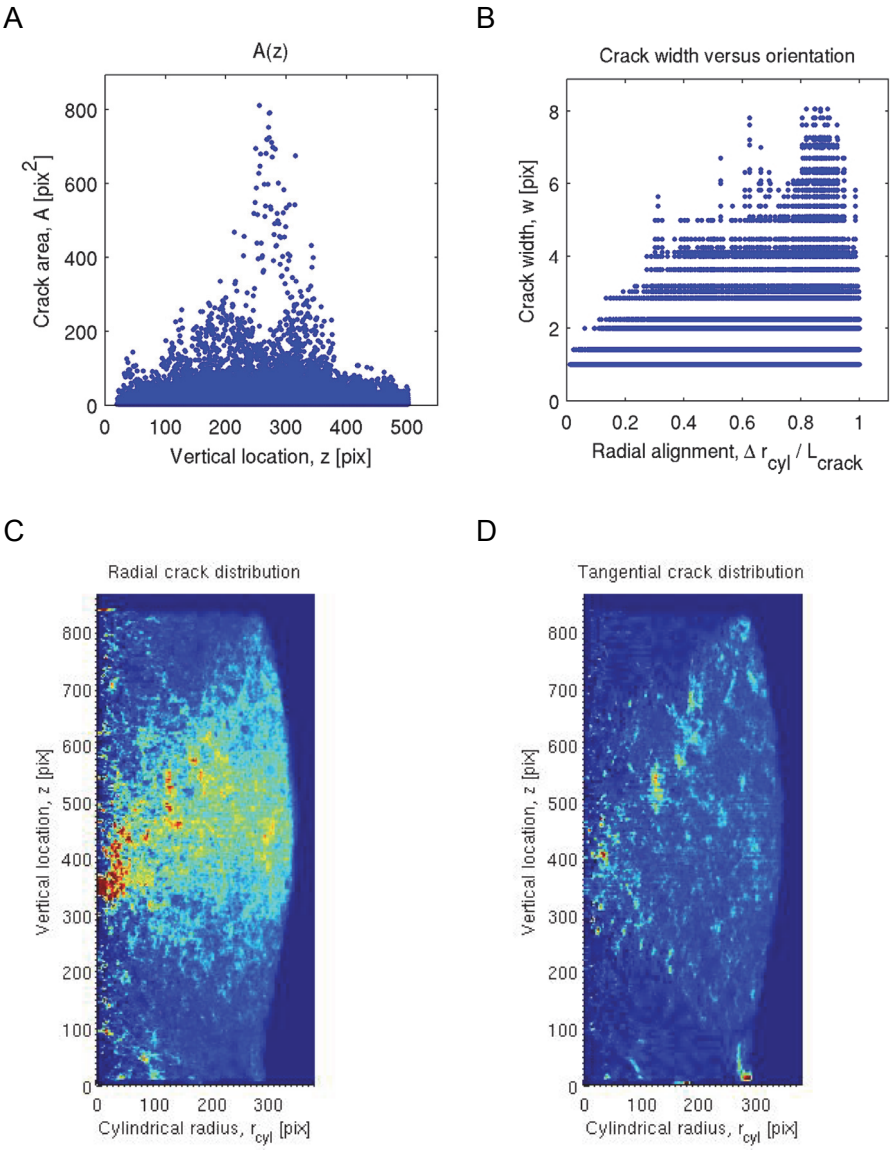

Figure S8. Quantification of fracture dimension and their position. (A) The fracture area increases near the centre of the barrelled sample, and (B) the width of extensional fractures widens near the margin. The half space images show the density of C) extensional and D) tangential (shear) fractures (colour coded where red is heavily fractured and blue is intact) collapsed onto the sample half space.

8.2. Fractures produced during deformation under an applied stress of 76 MPa

The analysis introduced for the symmetrical sample deformed under 28.5 MPa (i.e., Fig S8) cannot be entirely used for the sample deformed under 76 MPa because of the size of the fractures. Instead, we can compare the density of fractures within a half space (Fig S9). Unlike deformation at an applied stress of 28.5 MPa, which causes a widespread distribution of fractures (Fig S9A), deformation at 76 MPa is characterized by a strong localization of fractures parallel to the shear zone (Fig S9B). The fractures define an hourglass shape and the outside material shows a very high density of fracture. The angle of the hourglass shapes was observed to increasingly align with the direction of applied stress at higher stresses.

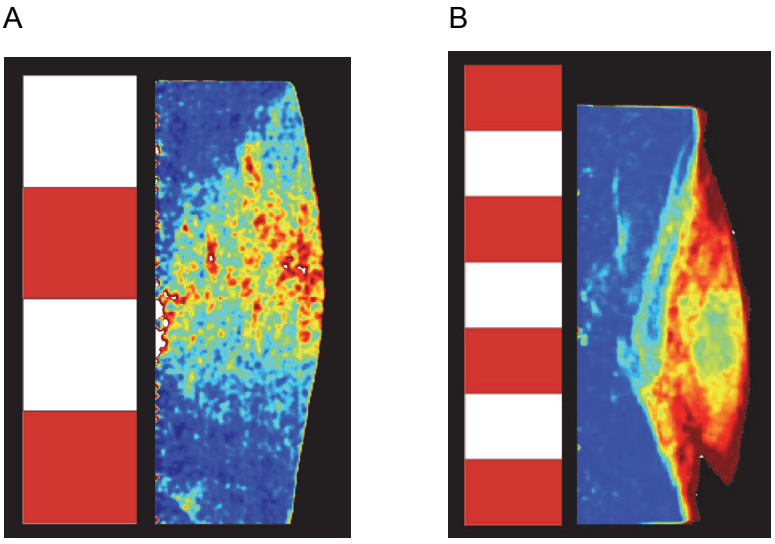

Figure S9. Fracture density in deformed magmas. The density of fractures (colour coded where red is heavily fractured and dark blue is intact) collapse within the half space of the samples deformed at A) 28.5 MPa and B) 76 MPa. Every red and white square vertically scales to 1 cm.

9. PERMEABILITY ANALYSIS

The permeability (κ) of lava dome rocks can be approximated through their porosity (ϕ) as they yield the following (Mueller et al., 2005):

$$\kappa = 10^{-17}\varphi^{3.4} \quad (4).$$

This relationship combined with the crack densities imaged by NCT (Bai et al., 2011; Hess et al., 2011; e.g., Pan et al., 2010) can thus provide a first order map of the permeability development during magma failure. Although the total porosity increases by cracking were comparable and led to similar bulk permeability increase (Table S2), analysis of the directional crack density from the NCT results highlighted contrasting anisotropy of the fracture networks in the different experiments. Flow in an anisotropic medium is very sensitive to fracture intensity (P) that defines the number of fractures expressed as

$$P = A_F/V \quad (5)$$

where A_F is the total area of the fracture contained in a volume (V) (Pan et al., 2010). The parameter P defines the number of fracture per unit length and is scale invariant (Ortega et al., 2006). When considering the anisotropy of a fracture network with a known volume, such as in our experimental

samples, the fracture intensities in the axial (a) and lateral (l) directions respectively scales with the surface area of cracks in each direction. Assuming that the surface area of fracture in a direction is a proxy for the permeable porosity in this direction – thus approximated by the ratio of area of fracture to considered surface area (A_T) – equation 4 can be reformulated to estimate the permeability along the axis of the samples (κ_a) and laterally across the sample (κ_l):

$$\kappa_a = 10^{-17}\left(\frac{A_{Fa}}{A_{Ta}}\right)^{3.4} \quad (6)$$

and

$$\kappa_l = 10^{-17}\left(\frac{A_{Fl}}{A_{Tl}}\right)^{3.4} \quad (7),$$

where A_{Fa}/A_{Ta} and A_{Fl}/A_{Tl} are estimated from tomography transects orthogonal to the axial and a radial direction, respectively (Fig S10).

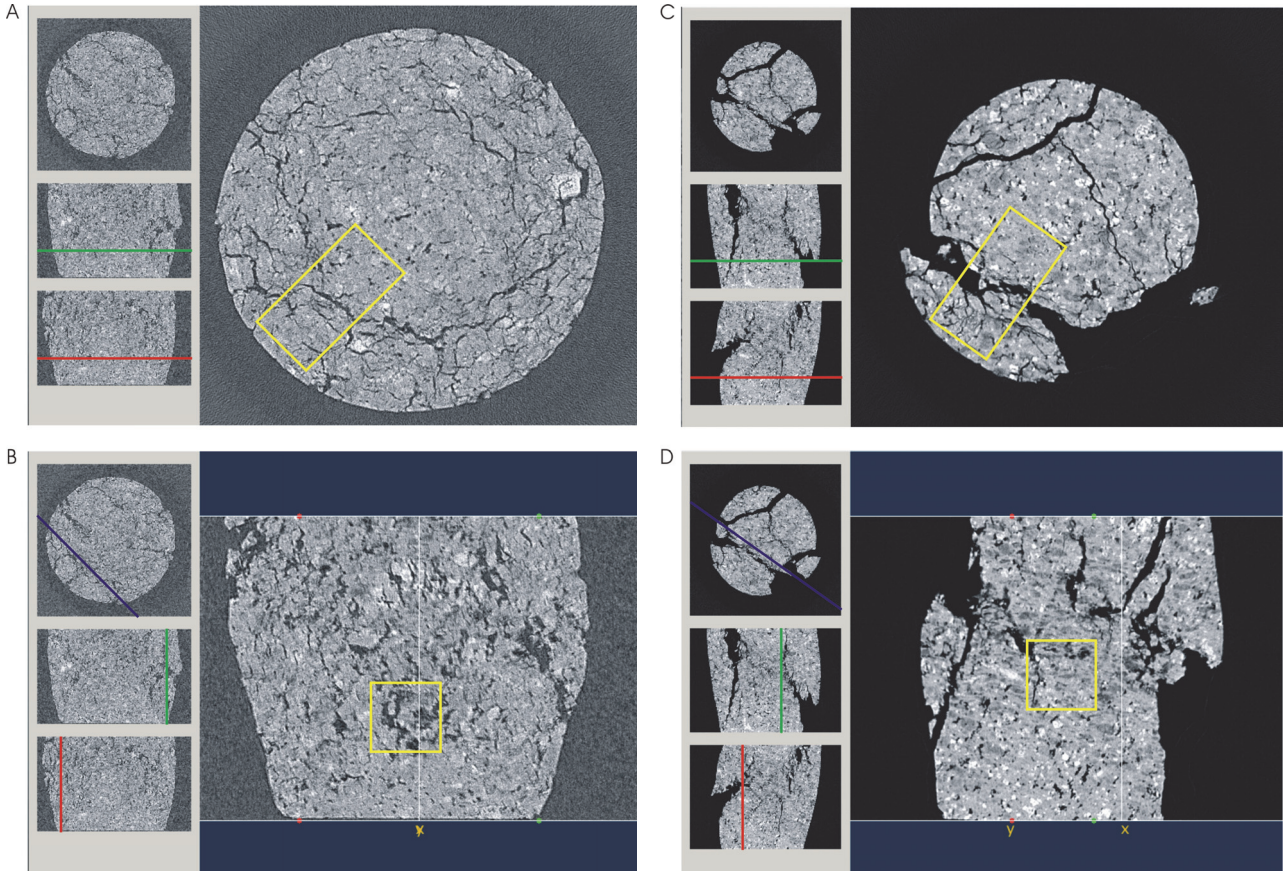

Figure S10. Reconstruction of the permeable fracture network. Regions from which the permeability was estimated across a segment of shear zone. The blue, green and red lines indicate the position of the sections of images displayed. A-B) The porosity of sample deformed at 28.5 MPa was estimated in a volume of 250 mm^3 (Yellow boxes). The analysis was performed in A) the axial direction of the sample, perpendicular to the applied stress, and in B) the radial direction, orthogonal to the applied stress. C-D) The porosity of sample deformed at 76 MPa was estimated in a volume of 250 mm^3 (Yellow boxes). The analysis was performed in C) the axial direction of the sample, perpendicular to the applied stress, and in D) the radial direction, orthogonal to the applied stress.

Tomographic sections were converted to binary images (pores and cracks were converted to black and the rock was converted to white) and the images were analysed with the JMicroVision toolbox (Roduit, 2006). The analysed porosities were then converted to permeabilities using equations 6 and 7 (Table S3).

Table S3. Permeability estimated on the basis of the porosity analysis. The data are plotted on Figure 2 in the main text.

Sample	Spatial analysis	Porosity	Permeability
28.5 MPa	*Bulk rock*	21 %	3.1×10^{-13}
	Axial	19.1%	2.3×10^{-13}
	Lateral	33.2	1.5×10^{-12}
76 MPa	*Bulk rock*	28 %	1.3×10^{-12}
	Axial	32.4 %	3.4×10^{-12}
	Lateral	16.0 %	1.2×10^{-13}

11. POST-EXPERIMENT MICROSTRUCTURAL ANALYSIS

The damage induced in the magma was further imaged using the traditional method of microscopic analysis. During thin section preparation, the rock samples were impregnated with epoxy doctored by the presence of a fluorescent dye in order to highlight the permeable, porous network (Fig S11). Mosaics of microphotographs (n>150) of the thin sections taken under reflected ultraviolet light illustrate at a high resolution the localisation of fractures during deformation at high applied stress (Fig S11 above). Moreover, the mosaics of the microphotographs taken under combined, reflected ultraviolet light and transmitted normal light display the relationship harboured between the propagation of fractures and the presence of phenocrysts (Fig S11 middle). We note that phenocrysts are especially fractured in material which have undergone a more significant amount of strain before ensuing to failure (i.e., at lower applied stress). (Fig S11 below).. This observation further leads us to suggest that during relatively “slow” failure (e.g., at an applied stress of 28.5 MPa) strain dissipate and is accommodated brittlely by phenocrysts, which crack and enhance the contribution to the permeable porous network, whereas during relatively “fast” failure (e.g., at an applied stress of 76 MPa), the development of cracks occurs (nearly) irrespective of the phenocrysts. From these observation, we conclude that the path dependence of failure (i.e., the total strain to failure) is material is strongly influenced by the presence of phenocrysts.

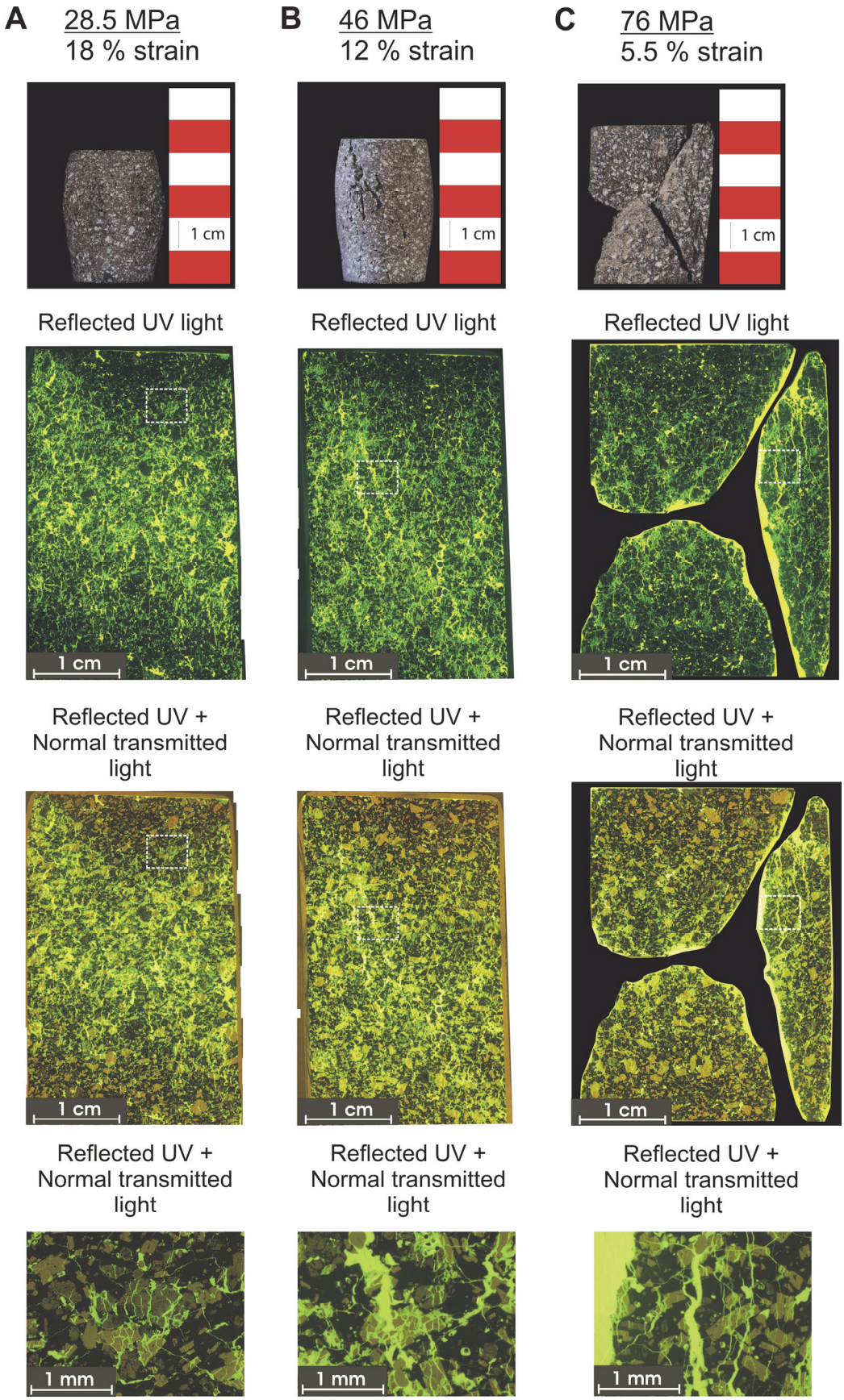

Figure S11. Microstructures produced during magma failure at A) 28.5 MPa, B) 46 MPa, and C) 76 MPa. The photograph of each sample is accompanied by a set mosaics of microphotographs taken under reflected UV light (above) and combined, reflected UV light and normal transmitted light (middle). These mosaics highlight the increase localisation of cracks with applied stress. Each mosaic further contains an inset box in which a high-resolution microphotographs display the relationship between cracking and the phenocrysts. [Note: for the sample deformed at 76 MPa, the localised macroscopic cracks prevented us from making one thin section for the rock, as the sample was very fragile. We thus prepared three different thin sections and reconstructed the sample geometry.]

SUPPLEMENTARY INFORMATION REFERENCES

Aki, K., 1965, Maximum likelihood estimate of b in the formula log N = a - bm and its confidence limits: Bulletin of the earthquake research institute, Tokyo University, v. 43, p. 237-239.

—, 1967, Scaling law of seismic spectrum: Journal of Geophysical Research, v. 72, p. 1217-&.

Bai, L.P., Baker, D.R., and Hill, R.J., 2011, Permeability of vesicular Stromboli basaltic glass: Lattice Boltzmann simulations and laboratory measurements: Journal of Geophysical Research-Solid Earth, v. 115.

Cornelius, R.R., and Voight, B., 1995, Graphical and Pc-Software Analysis of Volcano Eruption Precursors According to the Materials Failure Forecast Method (FFM): Journal of Volcanology and Geothermal Research, v. 64, p. 295-320.

Gerik, A., and Kruhl, J.H., 2008, Towards automated pattern quantification: time-efficient assessment of anisotropy of 2D patterns with AMOCADO: Computers and Geosciences.

Hess, K.U., Cordonnier, B., Lavallée, Y., and Dingwell, D.B., 2007, High-load, high-temperature deformation apparatus for synthetic and natural silicate melts: Review of Scientific Instruments, v. 78.

Hess, K.U., Flaws, A., Schillinger, B., Mühlbauer, M., Schulz, M., Calzada, E., and Dingwell, D.B., 2011, Applications of a high to ultra-high resolution neutron computed tomography system for the geosciences: Geological Society of America Bulletin, v. Advances in 3-D imaging and analysis of geomaterials.

Ketcham, R.A., and Carlson, W.D., 2001, Acquisition, optimization and interpretation of X-ray computed tomographic imagery: applications to the geosciences: Computers & Geosciences, v. 27, p. 381-400.

Kilburn, C.R.J., 2003, Multiscale fracturing as a key to forecasting volcanic eruptions: Journal of Volcanology and Geothermal Research, v. 125, p. 271-289.

King, A., Johnson, G., Engelberg, D., Ludwig, W., and Marrow, J., 2008, Observations of intergranular stress corrosion cracking in a grain-mapped polycrystal: Science, v. 321, p. 382-385.

Lavallée, Y., Benson, P.M., Heap, M.J., Flaws, A., Hess, K.U., and Dingwell, D.B., 2012a, Volcanic conduit failure as a trigger to magma fragmentation: Bulletin of Volcanology, v. 74, p. 11-13.

Lavallée, Y., Hess, K.U., Cordonnier, B., and Dingwell, D.B., 2007, A non-Newtonian rheological law for highly-crystalline dome lavas: Geology, v. 35, p. 843-846.

Lavallée, Y., Meredith, P., Dingwell, D.B., Hess, K.U., Wassermann, J., Cordonnier, B., Gerik, A., and Kruhl, J.H., 2008, Seismogenic lavas and explosive eruption forecasting: Nature, v. 453, p. 507-510.

Lavallée, Y., Varley, N., Alatorre-Ibargüengoitia, M.A., Hess, K.-U., Kueppers, U., Mueller, S., Richard, D., Scheu, B., Spieler, O., and Dingwell, D.B., 2012b, Magmatic Architecture of Dome-Building Eruptions at Volcán de Colima, Mexico: Bulletin of Volcanology, v. 74, p. 249-260.

Ma, C.M., and Sonka, M., 1996, A fully parallel 3D thinning algorithm and its applications: Computer Vision and Image Understanding, v. 64, p. 420-433.

McNutt, S.R., 2005, Volcanic seismology: Annual Review of Earth and Planetary Sciences, v. 33, p. 461-491.

Mueller, S., Melnik, O., Spieler, O., Scheu, B., and Dingwell, D.B., 2005, Permeability and degassing of dome lavas undergoing rapid decompression: An experimental determination: Bulletin of Volcanology, v. 67, p. 526-538.

Muhlbauer, M.J., Calzada, E., and Schillinger, B., 2005, Development of a system for neutron radiography and tomography, p. 324-328.

Ortega, O.J., Marrett, R.A., and Laubach, S.E., 2006, A scale-independent approach to fracture intensity and average spacing measurement: Aapg Bulletin, v. 90, p. 193-208.

Pan, J.-B., Lee, C.-C., Lee, C.-H., Yeh, H.-F., and Lin, H.-I., 2010, Application of fracture network model with crack permeability tensor on flow and transport in fractured rock: Engineering Geology, v. 116, p. 166-177.

Reubi, O., and Blundy, J., 2008, Assimilation of Plutonic Roots, Formation of High-K Exotic Melt Inclusions and Genesis of Andesitic Magmas at Volcán De Colima, Mexico: Journal of Petrology, v. 49, p. 2221-2243.

Roduit, N., 2006, JMicroVision: Image analysis toolbox for measuring and quantifying components of high-definition images.

Savov, I.P., Luhr, J.F., and Navarro-Ochoa, C., 2008, Petrology and geochemistry of lava and ash erupted from Volcan Colima, Mexico, during 1998-2005: Journal of Volcanology and Geothermal Research, v. 174, p. 241-256.

Smith, R., and Kilburn, C.R.J., 2010, Forecasting eruptions after long repose intervals from accelerating rates of rock fracture: The June 1991 eruption of Mount Pinatubo, Philippines: Journal of Volcanology and Geothermal Research, v. 191, p. 129-136.

Voight, B., 1988, A Method for Prediction of Volcanic-Eruptions: Nature, v. 332, p. 125-130.

Movie File

Click here to download Movie File: Video 1a-Colima - 28 MPa.gif

Movie File

Click here to download Movie File: Video 1b-Colima - 76 MPa.gif